Energy Advances

ROYAL SOCIETY OF CHEMISTRY

PAPER

View Article Online
View Journal | View Issue

Cite this: *Energy Adv.*, 2023, 2, 161

Facile surface reconstructions of cobalt–copper phosphide heterostructures enable efficient electrocatalytic glycerol oxidation for energy-saving hydrogen evolution†

Zhengzhe Xie,‡[a] Kang Wang,‡[b] Yu Zou,[a] Guobing Ying*[b] and Jiang Jiang*[a]

Received 14th November 2022,
Accepted 12th December 2022

DOI: 10.1039/d2ya00311b

rsc.li/energy-advances

The glycerol oxidation reaction (GOR) affords an energetically more favorable route for assisted H_2 production compared to the oxygen evolution reaction, with concurrent anodic value-added chemical generation. Herein, a self-supported CoP–Cu_3P composite on carbon cloth (CoP–Cu_3P/CC) has been fabricated, which exhibits excellent activity toward the GOR, requiring a low applied potential of 1.13 V (*vs.* reversible hydrogen electrode) to reach 10 mA cm^{-2}. Through combined surface elemental analysis, cyclic voltammetry, and *in situ* Raman spectroscopy characterizations, we reveal that metal elements in the mixed phosphide phases interact synergistically, leading to facilitated surface reconstruction and improved electrochemical activity. We further develop an electrolytic cell where the GOR is paired with the hydrogen evolution reaction using CoP–Cu_3P/CC as both the anode and cathode, which only needs the application of 1.21 V to reach a geometric current density of 10 mA cm^{-2}. This work provides a facile strategy to couple glycerol upgrading in an energy-saving water electrolysis system.

Introduction

Due to its high energy density and ultimate zero carbon emission, hydrogen is being considered as the most promising energy carrier for the future.[1] Renewable (green) hydrogen gas of high purity can be generated by electrochemical water splitting using intermittent energy supplies such as solar and wind power.[2–5] However, its commercialization is severely hindered by the high energy demand required to drive the thermodynamically uphill and kinetically sluggish anodic oxygen evolution reaction (OER).[6] Therefore, research endeavours have been focused on finding thermodynamically more favourable reactions to replace the anodic OER half-reaction in recent years, where electro-oxidation reactions of small organic molecules such as alcohol,[7–11] glycerol,[12–14] 5-hydroxymethylfurfural (HMF),[15–17] glucose,[18,19] and amines[20,21] have been applied as alternative oxidation half-reactions. By doing so, the overall voltage input for hydrogen evolution can be reduced significantly, the possible formation of an explosive O_2/H_2 gas mixture is avoided, and valuable chemicals are co-produced to further reduce the potential cost.[22–28]

Among the various small organic molecules, glycerol stands out as an attractive economically viable feedstock to assist the hydrogen evolution reaction (HER) due to several reasons: (1) glycerol oxidation reaction (GOR) requires a significantly lower thermodynamic oxidation potential (0.003 V *vs.* reversible hydrogen electrode, RHE) compared to the OER (1.23 V *vs.* RHE);[29] (2) a variety of high value-added products can be generated *via* selective glycerol oxidation;[30] (3) glycerol is a cheap by-product in over-supply from biodiesel and the soap industry.[31,32]

The most effective electrocatalysts for the GOR reported so far are often based on noble metals[33] such as Au, Pd, Pt and their alloys (PtBi and PdBi),[34,35] which suffer from high cost and poor stability against poisoning, making them less competitive for economically feasible hydrogen production. In recent reports, transition metal-based catalysts have shown great promise as alternatives to noble metals for the GOR in alkaline media, including transition metal oxides,[36–39] hydroxides,[40–44] and nitrides.[12,45,46] In particular, metal oxides and hydroxides containing both Co and Cu have demonstrated good activity toward the GOR.[47–49] Han *et al.*[47] conducted an investigation using cobalt-based spinel oxide (MCo_2O_4) as an electrocatalyst for the GOR, and discovered that $CuCo_2O_4$ was the best-performing catalyst with a high formate selectivity of ~80%.

[a] *i-Lab, CAS Key Laboratory of Nano-Bio Interface, Suzhou Institute of Nano-Tech and Nano-Bionics, Chinese Academy of Sciences, Suzhou 215123, China. E-mail: jjiang2010@sinano.ac.cn*
[b] *Department of Materials Science and Engineering, College of Mechanics and Materials, Hohai University, Nanjing 211100, China. E-mail: yinggb001@hhu.edu.cn*

† Electronic supplementary information (ESI) available: Additional figures and tables. See DOI: https://doi.org/10.1039/d2ya00311b

‡ These authors contributed equally.

Braun *et al.*[48] synthesized Cu–Co hydroxycarbonates $(Cu_{0.8}Co_{0.2})_2CO_3(OH)_2$ for alcohol oxidation reactions, and found that Cu leaching could lead to increased catalytic activity. Unfortunately, transition metal oxides and hydroxides are generally poor conductors, which may limit their electrocatalytic activity. On the other hand, given the metallic nature of transition metal phosphides (TMPs) and their ability to form a thin layer of metal (oxy)hydroxide in an oxidative environment,[50] TMPs have demonstrated superb activity toward water splitting applications.[51] However, TMPs have been rarely explored for glycerol oxidation reactions.

Herein, we have prepared self-supporting CoP–Cu_3P composite nanoarrays *via* transformation of mixed Co–Cu hydroxycarbonates. The self-supported structure can not only expose more active sites but also ensure good contact between the nanoarrays and the conductive substrate, accelerating the electron transport and mass transfer. We have found that the CoP–Cu_3P heterostructures result in modulated electronic structures, which facilitates facile surface reconstruction to generate high-valent Co species during the electrocatalytic process. The as prepared CoP–Cu_3P electrode only needs applied potentials of 1.13 and 1.22 V (*vs.* RHE) to drive geometric current densities of 10 and 20 mA cm^{-2} for the GOR in alkaline electrolyte (1 M KOH containing 0.1 M glycerol). Its practical feasibility is further demonstrated in an alkaline electrolyser using CoP–Cu_3P/CC as both the anode and cathode. A geometric current density of 10 mA cm^{-2} has been achieved at a low cell voltage of 1.21 V, 210 mV lower than what is required for conventional electrolytic overall water splitting.

Experimental

Materials

Copper nitrate trihydrate ($Cu(NO_3)_2{\cdot}3H_2O$, >99.0%), cobalt nitrate hexahydrate ($Co(NO_3)_2{\cdot}6H_2O$, 98.5%), ammonium fluoride (NH_4F, 96.0%), sodium hypophosphite monohydrate ($NaH_2PO_2{\cdot}H_2O$, >98.0%), urea ($CO(NH_2)_2$, 99.0%), acetone (99.5%), ethanol (99.7%), KOH (85.0%), HCl (36.0–38.0%) and glycerol (99.0%) were all obtained from Sinopharm Chemical Reagent Co., Ltd. All chemicals were used as received without purification. Carbon cloth (CC) was purchased from Shanghai Hesen Electric Co., Ltd. The deionized water was taken from a Millipore system.

Synthesis of Co–Cu hydroxycarbonates

$(Co,Cu)_2CO_3(OH)_2$/CC was synthesized *via* a hydrothermal reaction. To remove the organic impurities, carbon cloth was first cleaned sequentially using hydrochloric acid, deionized water, acetone, and ethanol. For a typical procedure, 1 mmol $Cu(NO_3)_2{\cdot}3H_2O$, 3 mmol $Co(NO_3)_2{\cdot}6H_2O$, 2 mmol NH_4F and 5 mmol urea were dissolved in 50 mL deionized water under magnetic stirring. The obtained transparent solution was then transferred into a Teflon-lined stainless steel autoclave (100 mL). Subsequently, a piece of carbon cloth (2 × 5 cm^2) was placed against the autoclave wall and immersed into the solution. The autoclave was then sealed and heated to 120 °C for a duration of 12 h. After that, the carbon cloth with sample grown on it was taken out of the autoclave, and rinsed thoroughly with deionized water. Mild ultrasonication was then applied in order to remove weakly surface bound hydroxycarbonates on the carbon cloth substrate. Finally, the $(Co,Cu)_2CO_3(OH)_2$/CC was left to dry at 70 °C in a vacuum oven for 12 h.

The synthetic procedures for $Co(CO_3)_{0.5}(OH){\cdot}0.11H_2O$/CC and $Cu_2(CO_3)(OH)_2$/CC were the same as that of $(Co,Cu)_2CO_3(OH)_2$/CC, except using $Co(NO_3)_2{\cdot}6H_2O$ or $Cu(NO_3)_2{\cdot}3H_2O$ as the only precursor during the hydrothermal reaction.

Synthesis of Co–Cu phosphides

Prior to the synthesis of phosphides, carbon cloth was first cut into 1 × 2 cm^2 pieces. In a typical phosphidation procedure, $NaH_2PO_2{\cdot}H_2O$ (1 g) was placed in a ceramic boat inside a quartz tube at the upstream position of the gas flow relative to a piece of carbon cloth (with corresponding metal hydroxycarbonates). After purging with N_2, the furnace was heated up to 300 °C at 5 °C min^{-1} ramping rate, and remained for 1 h.

Material characterizations

The prepared electrode morphologies were acquired using scanning electron microscopy operated at 10 kV (SEM, JEOL JSM-7500F), and transmission electron microscopy at an accelerating voltage of 200 kV (TEM, FEI Tecnai G2 F20 S-Twin). For TEM characterizations, the samples were first detached from the carbon cloth, redispersed in deionized water under ultrasonication, and then deposited on a Cu or Ni grid. The crystalline structure of the electrodes was surveyed using X-ray diffraction (XRD) on a Bruker D8 advance (Cu Kα radiation, 40 kV and 40 mA, scan speed 0.1° s^{-1}). The catalyst surface composition and valence states were investigated by X-ray photoelectron spectroscopy (XPS) on a Thermo Scientific K-Alpha (Al Kα X-ray source, 1486.6 eV). *In situ* Raman spectra were acquired on a Renishaw Raman InVia microscope with a home-designed electrochemical cell, using a 785 nm laser as the excitation source with a 50× objective lens.

Electrochemical measurements

The electrocatalytic performance for the GOR was tested by applying a three-electrode system on an electrochemical workstation (CHI 760E, Shanghai Chenhua Instrument Co., Ltd) at room temperature. The working electrodes were fabricated directly using the as-synthesized phosphide nanostructures grown on carbon cloth. For all electrochemical measurements, Hg/HgO (1 M KOH) was used as the reference electrode, and Pt foil was set as the counter electrode. The GOR was performed in 1 M KOH solution (25 mL) containing 0.1 M glycerol. Prior to recording electrochemical tests, activation processes were first conducted by continuous cyclic voltammogram (CV). Linear sweep voltammetry (LSV) was obtained by positively scanning the potential at a rate of 2 mV s^{-1} under stirring. By performing CV in the non-faradaic potential windows with different scanning rates, electrochemical double layer capacitance (C_{dl}) of the

electrodes was determined, which was then used to infer the electrochemical active surface area (ECSA). Electrochemical impedance spectroscopy (EIS) was performed with 5 mV amplitude in the frequency range from 0.1 Hz to 100 kHz. All the denoted potentials were referenced to the reversible hydrogen electrode (RHE) according to the following equation: $E_{RHE} = E_{Hg/HgO} + 0.059 \times pH + 0.098$. The iR-corrected LSV curves were plotted using solution resistance that has been determined from EIS measurements.

Two-electrode glycerol electrolysis was conducted using CoP–Cu_3P/CC as both the anode and cathode, with the LSV curves recorded at a sweep rate of 2 mV s^{-1}.

Product analysis

The products from the GOR were separated and quantified by high-performance liquid chromatography (HPLC) using an UltiMate 3000 (Thermo Fisher Scientific). For the HPLC measurements, aliquots of electrolyte solution (500 μL) extracted from the H-type cell were diluted by H_2SO_4 (0.5 M, 1.5 mL), and 20 μL of this diluted solution was then injected directly into a ChromCore Sugar-10H column. The eluent was H_2SO_4 solution (5 mM) at a 0.5 mL min^{-1} flow rate. For the individual GOR product, standard calibration curves were first obtained using sample solutions of known concentrations, as demonstrated in our previous work.[52]

Calculations of faradaic efficiency (FE) for the GOR are performed using the following half-reactions, which correspond to the oxidation of glycerol ($C_3H_8O_3$) into various products (glycerate: $C_3H_5O_4^-$; glycolate: $C_2H_3O_3^-$; oxalate: $C_2O_4^{2-}$; formate: $HCOO^-$) in alkaline solution:

$$C_3H_8O_3 + 5OH^- \rightarrow C_3H_5O_4^- + 4H_2O + 4e^- \quad (1)$$

$$C_3H_8O_3 + \frac{13}{2}OH^- \rightarrow \frac{3}{2}C_2H_3O_3^- + 5H_2O + 5e^- \quad (2)$$

$$C_3H_8O_3 + 14OH^- \rightarrow \frac{3}{2}C_2O_4^{2-} + 11H_2O + 11e^- \quad (3)$$

$$C_3H_8O_3 + 11OH^- \rightarrow 3HCOO^- + 8H_2O + 8e^- \quad (4)$$

The overall FE toward all products is calculated based on the following equation:

$$FE_{product} = \frac{Q_{product} \times C_{product} \times V \times F}{Q_{total}} \times 100 \quad (5)$$

in which $Q_{product}$ indicates the required charges to transform glycerol to a specific product, $C_{product}$ denotes the concentration of the product (mol L^{-1}), V is the electrolyte solution volume (0.025 L), F stands for Faraday's constant (96 485 C mol^{-1}), and Q_{total} represents the total passed charges (C).

Results and discussion

Cobalt–copper phosphide synthesis and characterization

Various methods for synthesizing TMPs have been developed, including electrodeposition,[53] vapor-phase deposition,[54] and solid phase reaction.[55] In order to expose more active sites, we synthesized a self-supported mixed Co–Cu phosphide nanostructure electrode *via* a two-step procedure (schematically shown in Fig. 1a), where Co–Cu hydroxycarbonate precursors on carbon cloth were formed first through hydrothermal reaction, and then subjected to a phosphidation reaction at 300 °C for 1 h in a ceramic boat under a phosphine atmosphere. For comparative studies, self-supported single phase cobalt phosphides and copper phosphides from their corresponding hydroxycarbonates were also prepared in the same way.

The structures of the as-formed Co–Cu hydroxycarbonate precursors and the corresponding metal phosphides scratched from the carbon cloth substrate were examined by powder XRD. The diffractogram of Co–Cu hydroxycarbonates showed peaks at 20.2, 24.1, 26.4, 33.6, and 39.0 degrees (as displayed in Fig. 1b), which can be indexed to the (001), (111), (220), (221), and (231) planes in the orthorhombic $(Co,Cu)_2CO_3(OH)_2$ phase (JCPDS No. 48-0084), matching well with the literature reports on Co–Cu hydroxycarbonates.[48,56] After annealing under a phosphine atmosphere, two new sets of XRD peaks appeared in the obtained sample. The diffraction peaks at 31.6° and 48.1° could be assigned to the (011) and (211) planes of CoP (JCPDS No. 29-0497), while those that appeared at 36.0, 39.1, 41.6, 45.1, and 46.2 degrees corresponded well to the diffractions from the (112), (202), (211), (300), and (113) planes of Cu_3P (JCPDS No. 71-2261), respectively. Using the same synthetic protocol, pure CoP and Cu_3P were also made by phosphiding the $Co(CO_3)_{0.5}(OH)\cdot 0.11H_2O$ and $Cu_2(CO_3)(OH)_2$ precursors, respectively. The XRD patterns confirmed the successful synthesis of single-phase CoP and Cu_3P (Fig. S1, ESI†), which served as control samples.

Under SEM, the $(Co,Cu)_2CO_3(OH)_2$ precursor was in the form of bundles of nanowires on the carbon cloth substrate (Fig. S2, ESI†). After phosphidation conversion, the morphology of the initial self-supported mixed Co–Cu hydroxycarbonates has been preserved well, as indicated in the respective SEM (Fig. 1c) and TEM (Fig. 1d) images. Generally speaking, a self-supporting structure is beneficial for enhanced electrocatalysis, *via* exposing active sites and facilitating rapid mass transfer. Finer detailed structures of the CoP–Cu_3P nanowires peeling off from the carbon cloth were revealed under high-resolution TEM (HRTEM). The distinct lattice fringes with 0.189 nm spacing can be ascribed to the (211) plane of orthorhombic CoP, and the ones with 0.249 nm spacing were in accordance with the (112) plane of hexagonal Cu_3P (Fig. 1e), matching well with the XRD results. Furthermore, elemental mapping by energy dispersive spectroscopy (EDS) confirmed the presence of Co (yellow), Cu (blue), and P (red), with all the elements homogeneously and uniformly distributed across the selected area (Fig. 1f), indicating abundant heterojunctions between CoP and Cu_3P. From the EDS spectrum (Fig. S3, ESI†), the Co/Cu molar ratio in CoP–Cu_3P was determined to be ~2.6, close to the initial feeding ratio of 3.

The surface elemental composition and valence states of the CoP–Cu_3P nanostructures were further characterized by XPS. The Co 2p, Cu 2p, P 2p, and O 1s peaks were clearly revealed in

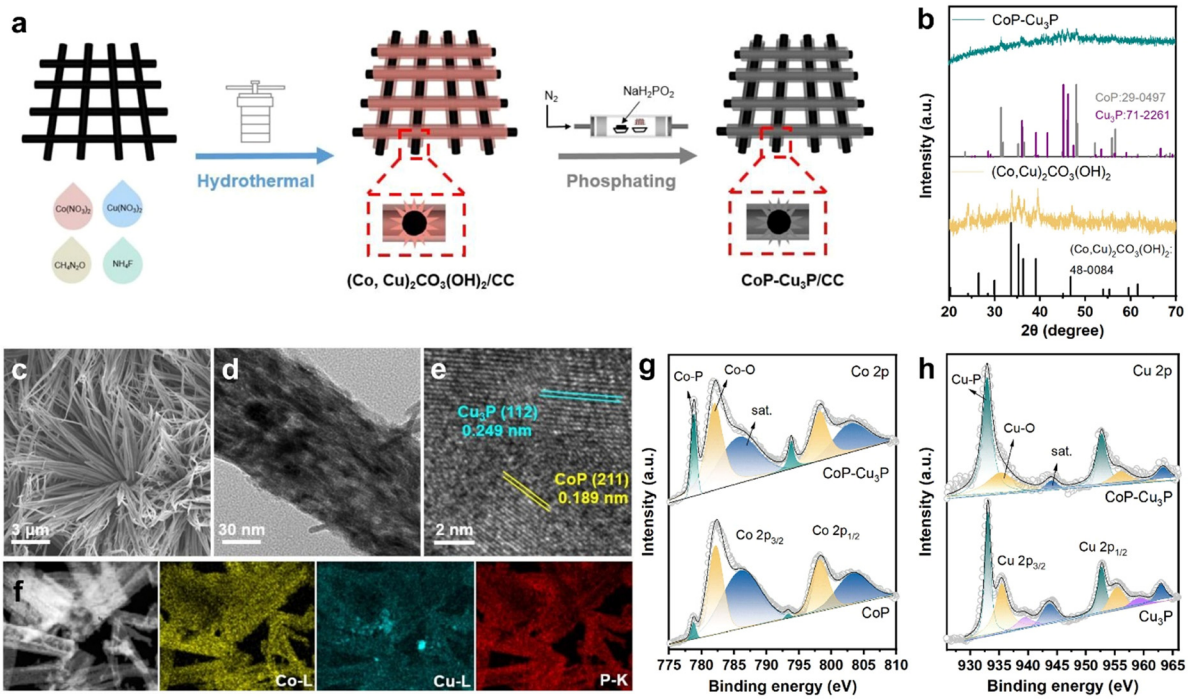

Fig. 1 (a) Schematic illustration of the procedures to produce mixed metal phosphides CoP–Cu_3P/CC. (b) XRD patterns of Co–Cu hydroxycarbonates $(Co,Cu)_2CO_3(OH)_2$ and CoP–Cu_3P. (c) SEM, (d) TEM, and (e) HRTEM images of CoP–Cu_3P. (f) Scanning transmission electron microscopy (STEM) image and energy dispersive spectroscopy (EDS) elemental mapping of Co, Cu and P elements in CoP–Cu_3P. (g) High resolution Co 2p XPS spectra of CoP and CoP–Cu_3P. (h) High resolution Cu 2p XPS spectra of Cu_3P and CoP–Cu_3P.

the XPS survey spectrum of CoP–Cu_3P, indicating the existence of the respective elements in the sample (Fig. S4a, ESI†). In the high-resolution Co 2p region of CoP and CoP–Cu_3P (Fig. 1g), the broad peaks at 778.8 eV and 793.8 eV were attributed to metallic state (Co^0) in CoP due to spin–orbit coupling effects, consistent with previous reports on the XPS of cobalt phosphides.[50,57,58] Furthermore, the peaks that appeared at 782.1/797.1 eV and 786.3/802.7 eV can be ascribed to the surface oxidized Co species and the satellite peaks, respectively.[59] For the high-resolution Cu 2p of Cu_3P and CoP–Cu_3P (Fig. 1h), the peaks at 933.1 eV and 952.8 eV are ascribed to Cu $2p_{3/2}$ and $2p_{1/2}$ in Cu_3P. The peaks at 935.5, 939.4, and 943.7 eV (satellite) as well as 955.4, 959.3, and 963.6 eV corresponded to the surface oxidized copper species.[60] Moreover, for the profile of the P 2p spectra of CoP, Cu_3P, and CoP–Cu_3P (Fig. S4b–d, ESI†), the characteristic peaks at around 129.5, 130.4, and 134.4 eV can be ascribed to P $2p_{3/2}$ and P $2p_{1/2}$ in the phosphides and the oxidized species such as PO_4^{3-} or P_2O_5, respectively. In addition, in single-phase CoP, the Co $2p_{3/2}$ peak (778.7 eV) was shifted positively from metallic Co (778.3 eV), while the P $2p_{3/2}$ peak (129.3 eV) had a smaller binding energy compared to P (130.1 eV), suggesting that Co possessed positive charge while P possessed negative charge. Similarly, in single-phase Cu_3P, the Cu $2p_{3/2}$ peak (933.1 eV) was also shifted positively from metallic Cu (932.6 eV), while the P $2p_{3/2}$ peak (129.0 eV) was shifted negatively from red P (130.1 eV), which also indicated that Cu and P possessed positive and negative charges, respectively. As shown in Fig. 1g and h, compared to the single-phase CoP and Cu_3P, the Co $2p_{3/2}$ and Cu $2p_{3/2}$ binding energies in CoP–Cu_3P were shifted positively to 778.8 and 932.9 eV, respectively. Furthermore, the P $2p_{3/2}$ and P $2p_{1/2}$ binding energies in CoP–Cu_3P also displayed positive shifts relative to those in CoP and Cu_3P (Fig. S4, ESI†). These results suggested that the electronic structures were modified for the CoP–Cu_3P nanocomposites, due to interfacial charge transfer between CoP and Cu_3P.

Electrocatalytic glycerol oxidation activity

After the successful synthesis of self-supporting CoP–Cu_3P nanowire arrays, their electrocatalytic activities for the GOR under alkaline conditions were then investigated in a single-compartment cell with the three-electrode configuration at room temperature. Given that water oxidation is the main competing anodic reaction, the OER was evaluated for comparison purposes, by keeping all other experimental conditions the same except without adding glycerol.

Prior to the actual electrochemical catalytic experiments, CoP–Cu_3P/CC was first electrochemically activated by continuous cyclic voltammetry (reaching equilibrium after 4–5 cycles, Fig. S5, ESI†), and then LSV was recorded in 1 M KOH solution with 0.1 M glycerol. As shown in Fig. 2a (cyan solid line), the CoP–Cu_3P/CC is highly active toward the glycerol oxidation reaction, requiring a potential of only 1.13 and 1.22 V (*vs.* RHE, unless otherwise noted) to achieve a geometric current density of 10 and 20 mA cm^{-2}, respectively. In the absence of glycerol, CoP–Cu_3P/CC can also catalyze electrochemical water

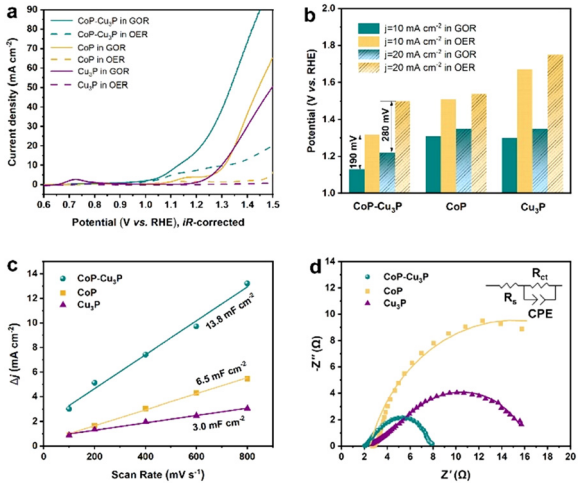

Fig. 2 (a) LSV curves of CoP, Cu_3P, and CoP–Cu_3P grown on carbon cloth in 1 M KOH solution with (solid lines) and without (dashed lines) 0.1 M glycerol addition. (b) Comparison of the applied potential at 10 and 20 mA cm^{-2} for various electrodes under GOR and OER conditions. (c) Estimation of the ECSA of various electrodes based on C_{dl} values extracted from CV measurements in the non-faradaic regions. (d) Nyquist plots of various electrodes from EIS measurements performed at onset potentials.

oxidation (Fig. 2a, cyan dashed line), but at considerably more positive potentials, requiring a potential of 1.32 and 1.50 V to drive the same geometric current density of 10 and 20 mA cm^{-2}. Moreover, comparative studies using CoP were also conducted under GOR and OER conditions (Fig. 2a, yellow solid and dashed lines), showing only moderate electrocatalytic activities. Cu_3P displayed similar electrochemical activities toward the GOR compared to that of CoP. Under all the tested conditions, the GOR is electrochemically more favorable than the OER. In Fig. 2b, the anodic potentials to drive the glycerol oxidation reaction and water oxidation reaction at a geometric current density of 10 and 20 mA cm^{-2} were plotted together for comparison, showing 190 or 280 mV reduction in the driving potentials to reach a geometric current density of 10 or 20 mA cm^{-2} when switching the OER to the GOR using CoP–Cu_3P/CC as the electrocatalyst. The measured GOR activity of CoP–Cu_3P/CC in 1 M KOH solution containing 0.1 M glycerol is comparable or even slightly better than some recently reported state of the art precious-metal-free GOR electrocatalysts, such as $CuCo_2O_4$ (1.30 V),[47] Ni–Mo–N (1.30 V),[12] and NiO_x/MWCNTs (1.31 V).[38] A more complete comparison with recent literature reports is tabulated in Table S1 (ESI†). LSV curves on $(Co,Cu)_2CO_3(OH)_2$ precursors were also recorded for comparison, which exhibited very poor activity toward the electrocatalytic GOR, requiring an applied potential of 1.92 V to reach a current density of 10 mA cm^{-2} (Fig. S6, ESI†). We also varied the feeding ratio of Co/Cu in preparing the mixed Co–Cu phosphides to 1 : 1 and 1 : 3, and the resulting Co–Cu phosphides had lost the original nanowire morphology, and also displayed worse performance in the GOR than CoP–Cu_3P nanocomposites with 3 : 1 Co/Cu feeding ratio (Fig. S7, ESI†).

To understand the synergistically enhanced electrochemical GOR activity of CoP–Cu_3P, we first compared their respective electrochemical surface area (ECSA). The ECSA was determined from the measured double-layer capacitance (C_{dl}) using cyclic voltammetry (Fig. S8, ESI†). As shown in Fig. 2c, the CoP–Cu_3P nanocomposite possesses a considerably higher $2C_{dl}$ (13.8 mF cm^{-2}) than CoP (6.5 mF cm^{-2}) and Cu_3P (3.0 mF cm^{-2}), suggesting that the formation of nanocomposites resulted in more exposed active sites, which are beneficial to achieve high electrocatalytic GOR activity. Electrochemical impedance spectroscopy (EIS) measurement was then conducted to evaluate the charge transfer kinetics on CoP, Cu_3P, and CoP–Cu_3P during the GOR process (Fig. 2d). The EIS spectra show that these phosphide catalysts displayed similar solution resistances (R_s), but quite different charge transfer resistances (R_{ct}). The CoP–Cu_3P nanocomposite showed much smaller charge transfer resistance R_{ct} of 5.70 Ω, compared to that of CoP (22.69 Ω) and Cu_3P (17.78 Ω), indicating that the charge transfer kinetics are facilitated by forming a CoP–Cu_3P heterostructure. Therefore, both increased active surface area and faster charge transfer kinetics contributed to the enhanced activity of the CoP–Cu_3P nanocomposite toward the GOR.

Surface reconstructions of CoP–Cu_3P during electrocatalysis

TMPs are often considered as the pre-catalyst in electrochemical oxidation reactions, as the surfaces of metal phosphides are converted to metal (oxy)hydroxides, which serve as the actual catalysts.[50,61,62] To investigate the structural evolution and stability of the CoP–Cu_3P catalyst, morphological examination under SEM and TEM was conducted after the electrochemical glycerol oxidation reactions. The SEM image (Fig. S9a, ESI†) demonstrates that the nanowire morphology of CoP–Cu_3P was largely maintained after the GOR process. More detailed surface morphology was surveyed by carrying out TEM measurement. As shown in Fig. S9b (ESI†), a thin amorphous surface layer of 6–8 nm appeared to cover the inner crystalline nanowire, which not only served as the catalytic center but also protected the underlying metal phosphides from further oxidation. Moreover, the XRD pattern of CoP–Cu_3P after the GOR confirmed the formation of cobalt oxyhydroxide. As shown in Fig. S10 (ESI†), the newly appeared diffraction peaks at 36.9°, 38.2°, and 65.7° could be assigned to the (021), (040), and (002) planes in CoOOH (JCPDS No. 26-0480), respectively. The surface composition and valence states of the CoP–Cu_3P catalyst after the GOR were further examined by XPS. For both CoP–Cu_3P and CoP, the peaks of Co^0 species disappeared after the GOR, while Co^{3+} emerged in the high-resolution Co 2p spectra (Fig. S11a, ESI†). This indicates that near-surface Co^0 species were oxidized to a higher valence state, forming a surface oxide-rich layer during the GOR process. In addition, the Co $2p_{3/2}$ spectra showed lower binding energy (0.6 eV) of Co^{3+} in CoP–Cu_3P compared to that in CoP, suggesting possible electron transfer from Cu_3P to CoP. Fig. S11b (ESI†) displays the high-resolution XPS spectrum of Cu 2p, with peaks for Cu–P bonds remaining. Moreover, the Cu 2p binding energy exhibited an upward shift (0.23 eV) for Cu–P in CoP–Cu_3P, in comparison to that of Cu_3P. The observed opposite shifts in Co and Cu binding energies suggested that interfacial charge transfer

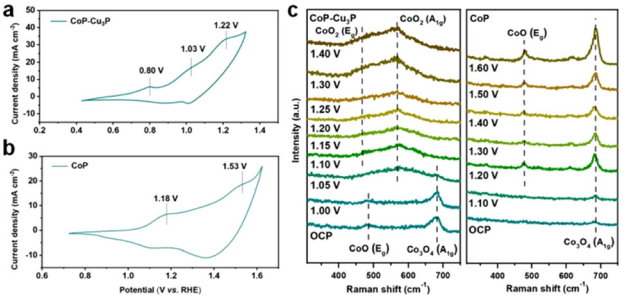

Fig. 3 (a) CV curve in the potential range of 0.4–1.3 V *vs.* RHE of CoP–Cu_3P, with a scan rate of 5 mV s^{-1}. (b) CV curve in the potential range of 0.7–1.6 V *vs.* RHE of CoP, with a scan rate of 5 mV s^{-1}. (c) *In situ* Raman spectroscopy conducted on the CoP–Cu_3P electrode at increasing applied potentials from OCP to 1.4 V (left) and on the CoP electrode at increasing applied potentials from OCP to 1.6 V (right).

occurred between CoP and Cu_3P in the mixed bimetallic phosphide heterostructures. Heterostructures with modulated interfacial electronic structures have been demonstrated to be active electrocatalysts toward various reactions.[63–67]

CV and *in situ* Raman spectroscopy measurements provided more evidence and insight into the surface oxidation and reconstruction behaviors of TMPs. As shown in Fig. 3a, three anodic peaks at 0.80, 1.03, and 1.22 V, which correspond to the oxidation of Cu and Co (Co^{2+}/Co^{3+} and Co^{3+}/Co^{4+} redox pairs), were observed in the cyclic voltammogram of CoP–Cu_3P. For pure Cu_3P, the anodic oxidation peak appeared at 0.82 V, close to that in the CoP–Cu_3P nanocomposites (Fig. S12a, ESI†). However, the cyclic voltammogram of pure CoP displayed a significant anodic shift of the Co oxidation peaks, with Co^{2+}/Co^{3+} and Co^{3+}/Co^{4+} oxidation occurring at 1.18 and 1.53 V, respectively (Fig. 3b). This is also consistent with the observed negative Co^{3+} binding energy shift. Given that the high-valency Co species (Co^{3+}/Co^{4+}) have been suggested to be involved actively in water oxidation, biomass and glycerol oxidation reactions,[68–70] we postulate that the facile generation of high-valent Co species on the surface of CoP–Cu_3P is likely the key to achieving efficient GOR. This is confirmed by *in situ* Raman spectroscopic characterizations. Fig. 3c shows the *in situ* Raman spectra that had been recorded on CoP–Cu_3P in 1 M KOH, scanning at a rate of 1 mV s^{-1} from the open circuit potential (OCP) to 1.40 V. Two broad peaks located at 484 and 691 cm^{-1}, corresponding to the E_g vibrational mode of Co–O and A_{1g} vibrational mode of Co_3O_4, were observed at OCP. The appearance of CoO_x on the catalyst surface is due to oxidation by the electrochemical activation treatment, which is common for metal phosphides.[71–73] After the applied potential was raised above 1.05 V, new peaks started to emerge at 474 and 572 cm^{-1}, which can be ascribed to the E_g and A_{1g} vibrational modes of CoO_2, accompanied by the disappearance of E_g and A_{1g} vibrational modes of CoO and Co_3O_4. This indicated that a chemical conversion process on CoP–Cu_3P started to occur from 1.05 V, generating new amorphous surface species with high-valent Co. As a control, *in situ* Raman spectroscopy was also conducted similarly on CoP and Cu_3P as a function of the applied potential. As displayed in Fig. 3c, a weak peak located at 691 cm^{-1} was present at OCP, which can be assigned to CoO_x on the CoP surface. Two new peaks at 484 and 608 cm^{-1} emerged from 1.2 V onward, together with the peak at 691 cm^{-1} showing increasing intensity, indicating more surface Co^{2+} and Co^{3+} generation. These results indicate that CoO_x on the CoP surface is electrochemically rather stable, with very little Co^{3+} generation and accumulation after the voltage exceeds 1.2 V. Surprisingly, no Raman signals were detected on Cu_3P, either at the OCP or upon raising the applied potential to 1.6 V (Fig. S12b, ESI†). A similar finding was reported by Zhou *et al.*,[74] but the exact reason remains elusive. Both redox behaviors in CV and the *in situ* Raman spectra support the conclusion that the CoP–Cu_3P surface is more readily reconstructed to produce high-valence surface Co^{3+} and Co^{4+} species in comparison to CoP, which is beneficial for the enhanced GOR activity.

Based on the above electrochemical, XPS, and *in situ* Raman characterization results, we therefore postulate that the excellent activity of the self-supporting CoP–Cu_3P heterostructures toward electrocatalytic glycerol oxidation reactions likely originates from multiple factors: (1) abundant exposed active sites; (2) improved charge transfer kinetics on metallic metal phosphides; (3) formation of surface high-valent cobalt acting as a catalytic center, facilitated by electron transfer across the bimetallic phosphide interface.

Glycerol oxidation selectivity and coupled hydrogen evolution reaction

Electrochemical oxidation of glycerol can be a very complex process with various possible intermediate products involved. In the following section, the GOR was conducted on CoP–Cu_3P/CC electrodes in an H-cell with a conventional three-electrode system, with the oxidation products quantitatively analyzed using HPLC. Typical HPLC chromatograms (Fig. S13, ESI†) display multiple elution peaks at retention times of 16.0, 14.5, 13.1, and 10.4 min, corresponding to formic acid, glycolic acid, glyceric acid, and oxalic acid, respectively. Calibration curves were obtained using pure chemicals with varying known concentrations, before the quantitative analysis of specific oxidation products (Fig. S14, ESI†). Holding the GOR at fixed applied potentials over a certain duration, the *I*–*t* data were acquired at 1.20, 1.30, 1.40 and 1.50 V (Fig. 4a), with oxidation products collected and analyzed to calculate the respective faradaic efficiencies. As shown in Fig. 4b, the total faradaic efficiency for all the detected solution products remained over 80% after 6 h of electrocatalysis at 1.2 V. When the applied potential was raised to 1.5 V, the overall faradaic efficiency dropped to ~60%. In terms of specific oxidation products, the faradaic efficiencies of oxalic acid and glycolic acid decreased, with a concomitant increase in that of formic acid, upon raising the applied potentials. At 1.5 V, formic acid and oxalic acid remained as the only detectable oxidation products in the solution. This can be understood by the respective stability of various glycerol oxidation products. On CoP–Cu_3P/CC electrodes, the electrochemical reactivity followed the order of glycerol > glycolic acid > formic acid > oxalic acid (Fig. S15, ESI†).

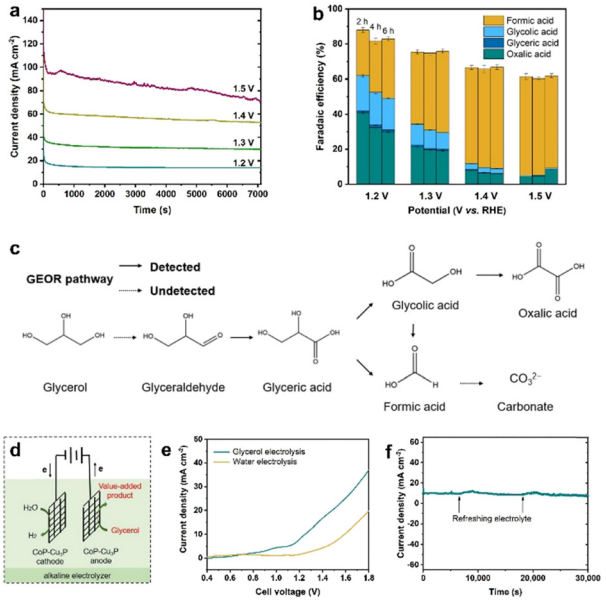

Fig. 4 (a) *I–t* curves of GOR performed at different applied potentials in 1 M KOH containing 0.1 M glycerol. (b) The faradaic efficiencies toward various solution oxidized products in the GOR at different applied potentials in 1 M KOH that contained 0.1 M glycerol. (c) Proposed reaction pathways over CoP–Cu_3P electrocatalysts for the GOR. (d) Schematic illustration of the two-electrode electrolysis system by integrating the GOR with the HER. (e) LSV curves for the CoP–Cu_3P/CC||CoP–Cu_3P/CC cell in 1.0 M KOH solution with and without 0.1 M glycerol addition. (f) *I–t* curve of the CoP–Cu_3P/CC||CoP–Cu_3P/CC cell with a constant applied potential of 1.21 V for 30 000 s; the arrows indicate addition of extra glycerol to refresh the electrolyte.

Upon increasing the applied potential, glycolic acid is likely to be oxidized further to oxalic acid or to formic acid by breaking the C–C bond, while formic acid may be further mineralized completely to CO_2 at sufficiently positive anodic potentials, thus resulting in reduced overall faradaic efficiency. We also analyzed the gaseous products using gas chromatography. However, no O_2 or CO_2 had been detected, indicating that the OER is not contributing to the lost faradaic efficiency, and the generated CO_2 was dissolved in alkaline electrolyte forming CO_3^{2-}. By assuming that the missing FE is solely due to the complete oxidation to CO_2, the glycerol conversion, oxidation product selectivity, and carbon balance have been calculated and shown in Fig. S16 (ESI†). The calculated carbon balance values remained all above 90% at different applied potentials. After electrolysis at 1.5 V over 6 h, 65% of the original glycerol was oxidized mainly to formate (68% selectivity) and CO_2, with only little oxalate and a trace amount of glycolic acid. Based on the above data, we propose a possible oxidation pathway for the electrocatalytic GOR on the CoP–Cu_3P nanocomposites (Fig. 4c). The initial oxidation took place selectively on the terminal hydroxyl group of glycerol to generate glyceraldehyde, which was subsequently oxidized to glyceric acid. Glyceric acid can undergo a further oxidation step, forming glycolic acid and formic acid *via* C–C bond cleavage. Meanwhile, glycolic acid can be directly oxidized to oxalic acid or oxidized to formic acid by C–C bond cleavage.

Finally, being inspired by the demonstrated high activity of metal phosphides toward hydrogen evolution,[55,75–77] we went on to evaluate the performance of the as-prepared CoP–Cu_3P/CC electrode for the HER in alkaline solution. As expected, the LSV profile of the CoP–Cu_3P/CC electrode exhibited high activity for the catalytic HER, requiring an overpotential of ~75 mV to reach a geometric current density of 10 mA cm^{-2} in 1 M KOH with or without glycerol (Fig. S17, ESI†). Given the demonstrated excellent activity of the CoP–Cu_3P catalyst toward both the HER and GOR, a two-electrode alkaline electrolyzer was assembled using CoP–Cu_3P/CC as both the cathode and anode for glycerol electrolysis (Fig. 4d). For comparison, the performance of the CoP–Cu_3P/CC||CoP–Cu_3P/CC electrolyzer for overall water splitting was also investigated in 1 M KOH electrolyte. As shown in Fig. 4e, a cell voltage of 1.42 V was required to drive 10 mA cm^{-2} in 1 M KOH solution. After the introduction of 0.1 M glycerol, the minimum required cell voltage to drive 10 mA cm^{-2} was reduced to 1.21 V, demonstrating that it is considerably more energy-efficient to produce hydrogen by replacing anodic oxygen evolution with glycerol oxidation. Actually, the current CoP–Cu_3P/CC electrode system has surpassed many of the previously reported energy-saving hydrogen evolution systems using alternative anode oxidation reactions to replace the conventional OER (Table S2, ESI†). Moreover, the CoP–Cu_3P/CC||CoP–Cu_3P/CC electrolyzer has been demonstrated to maintain excellent durability for coupled HER/GOR reactions, as suggested by the *I–t* curve shown in Fig. 4f.

Conclusions

In conclusion, we have successfully synthesized 3D binary phosphide nanowire arrays on carbon cloth (CoP–Cu_3P/CC) *via* transformation of mixed Co–Cu hydroxycarbonates. The as-synthesized self-supporting CoP–Cu_3P shows outstanding activity of catalyzing glycerol oxidation in the alkaline electrolyte, requiring a low applied potential of 1.13 V *vs.* RHE to yield 10 mA cm^{-2} in 1 M KOH solution with 0.1 M glycerol. Their enhanced electrocatalytic performance originates from the abundantly exposed active sites and excellent charge transfer characteristics. Through systematic investigation using XPS, CV, and *in situ* Raman, we have unveiled that the electronic interaction between CoP and Cu_3P leads to facile high-valent Co species generation during the electrocatalytic process. In addition, a two-electrode alkaline electrolyzer was assembled by employing CoP–Cu_3P/CC as both the cathode and anode for the HER/GOR. This electrolyzer requires only an impressively low voltage of 1.21 V to drive a geometric current density of 10 mA cm^{-2}. This work may provide guidance for designing advanced multiphase transition metal phosphide catalysts in the future, which can be used for glycerol as well as other organic electrooxidation-coupled electrolysis systems.

Author contributions

Zhengzhe Xie: methodology, validation, investigation, visualization, writing original draft; Kang Wang: methodology,

validation, investigation, visualization; Yu Zou: methodology, writing – review & editing; Guobing Ying: writing-review&editing, supervision; Jiang Jiang: conceptualization, writing – review & editing, supervision, funding acquisition.

Conflicts of interest

There are no conflicts to declare.

Acknowledgements

This work was funded by the Jiangsu Provincial Double-innovation Doctor Program (No. JSSCBS20211432) and the National Natural Science Foundation of China (No. 21873113). We thank Xin Huang for helping with the *in situ* Raman spectroscopy.

Notes and references

1 X. Tao, Y. Zhao, S. Wang, C. Li and R. Li, *Chem. Soc. Rev.*, 2022, **51**, 3561–3608.
2 Q. Zhang, N. M. Bedford, J. Pan, X. Lu and R. Amal, *Adv. Energy Mater.*, 2019, **9**, 1901312.
3 J. Zhu, L. Hu, P. Zhao, L. Y. S. Lee and K.-Y. Wong, *Chem. Rev.*, 2020, **120**, 851–918.
4 Z. Xie, W. Wang, D. Ding, Y. Zou, Y. Cui, L. Xu and J. Jiang, *J. Mater. Chem. A*, 2020, **8**, 12169–12176.
5 F. W. S. Lucas, R. G. Grim, S. A. Tacey, C. A. Downes, J. Hasse, A. M. Roman, C. A. Farberow, J. A. Schaidle and A. Holewinski, *ACS Energy Lett.*, 2021, **6**, 1205–1270.
6 L. Zhang, W. Cai and N. Bao, *Adv. Mater.*, 2021, **33**, 2100745.
7 G.-F. Chen, Y. Luo, L.-X. Ding and H. Wang, *ACS Catal.*, 2017, **8**, 526–530.
8 B. You, X. Liu, X. Liu and Y. Sun, *ACS Catal.*, 2017, **7**, 4564–4570.
9 X. Deng, M. Li, Y. Fan, L. Wang, X.-Z. Fu and J.-L. Luo, *Appl. Catal., B*, 2020, **278**, 119339.
10 D. Wu, J. Hao, W. Wang, Y. Yu, X. Z. Fu and J. L. Luo, *ChemSusChem*, 2021, **14**, 5450–5459.
11 Z. Li, Y. Yan, S. M. Xu, H. Zhou, M. Xu, L. Ma, M. Shao, X. Kong, B. Wang, L. Zheng and H. Duan, *Nat. Commun.*, 2022, **13**, 147.
12 Y. Li, X. Wei, L. Chen, J. Shi and M. He, *Nat. Commun.*, 2019, **10**, 5335.
13 L. Fan, Y. Ji, G. Wang, J. Chen, K. Chen, X. Liu and Z. Wen, *J. Am. Chem. Soc.*, 2022, **144**, 7224–7235.
14 X. Yu, E. C. Dos Santos, J. White, G. Salazar-Alvarez, L. G. M. Pettersson, A. Cornell and M. Johnsson, *Small*, 2021, **17**, 2104288.
15 B. You, X. Liu, N. Jiang and Y. Sun, *J. Am. Chem. Soc.*, 2016, **138**, 13639–13646.
16 G. Yang, Y. Jiao, H. Yan, Y. Xie, A. Wu, X. Dong, D. Guo, C. Tian and H. Fu, *Adv. Mater.*, 2020, **32**, 2000455.
17 T. Wang, Z. Huang, T. Liu, L. Tao, J. Tian, K. Gu, X. Wei, P. Zhou, L. Gan, S. Du, Y. Zou, R. Chen, Y. Li, X. Z. Fu and S. Wang, *Angew. Chem., Int. Ed.*, 2021, **61**, 202115636.
18 W. J. Liu, Z. Xu, D. Zhao, X. Q. Pan, H. C. Li, X. Hu, Z. Y. Fan, W. K. Wang, G. H. Zhao, S. Jin, G. W. Huber and H. Q. Yu, *Nat. Commun.*, 2020, **11**, 265.
19 Y. Zhang, B. Zhou, Z. Wei, W. Zhou, D. Wang, J. Tian, T. Wang, S. Zhao, J. Liu, L. Tao and S. Wang, *Adv. Mater.*, 2021, **33**, 2104791.
20 Y. Huang, X. Chong, C. Liu, Y. Liang and B. Zhang, *Angew. Chem., Int. Ed.*, 2018, **57**, 13163–13166.
21 X. Chong, C. Liu, C. Wang, R. Yang and B. Zhang, *Angew. Chem., Int. Ed.*, 2021, **60**, 22010–22016.
22 Y. Xu and B. Zhang, *ChemElectroChem*, 2019, **6**, 3214–3226.
23 B. Garlyyev, S. Xue, J. Fichtner, A. S. Bandarenka and C. Andronescu, *ChemSusChem*, 2020, **13**, 2513–2521.
24 Y. Holade, N. Tuleushova, S. Tingry, K. Servat, T. W. Napporn, H. Guesmi, D. Cornu and K. B. Kokoh, *Catal. Sci. Technol.*, 2020, **10**, 3071–3112.
25 Y. Li, X. Wei, L. Chen and J. Shi, *Angew. Chem., Int. Ed.*, 2021, **60**, 19550–19571.
26 J. Jack, W. Zhu, J. L. Avalos, J. Gong and Z. J. Ren, *Green Chem.*, 2021, **23**, 7917–7936.
27 C. Deng, C. Y. Toe, X. Li, J. Tan, H. Yang, Q. Hu and C. He, *Adv. Energy Mater.*, 2022, **12**, 2201047.
28 H. Luo, J. Barrio, N. Sunny, A. Li, L. Steier, N. Shah, I. E. L. Stephens and M. M. Titirici, *Adv. Energy Mater.*, 2021, **11**, 2101180.
29 M. Simoes, S. Baranton and C. Coutanceau, *ChemSusChem*, 2012, **5**, 2106–2124.
30 A. Behr, J. Eilting, K. Irawadi, J. Leschinski and F. Lindner, *Green Chem.*, 2008, **10**, 13–30.
31 G. Dodekatos, S. Schünemann and H. Tüysüz, *ACS Catal.*, 2018, **8**, 6301–6333.
32 L. Fan, B. Liu, X. Liu, N. Senthilkumar, G. Wang and Z. Wen, *Energy Technol.*, 2020, **9**, 2000804.
33 T. Li and D. A. Harrington, *ChemSusChem*, 2021, **14**, 1472–1495.
34 Y. Kwon, Y. Birdja, I. Spanos, P. Rodriguez and M. T. M. Koper, *ACS Catal.*, 2012, **2**, 759–764.
35 A. Zalineeva, A. Serov, M. Padilla, U. Martinez, K. Artyushkova, S. Baranton, C. Coutanceau and P. B. Atanassov, *J. Am. Chem. Soc.*, 2014, **136**, 3937–3945.
36 Y. Li, X. Wei, S. Han, L. Chen and J. Shi, *Angew. Chem., Int. Ed.*, 2021, **60**, 21464–21472.
37 P. V. B. Santiago, C. C. Lima, J. L. Bott-Neto, P. S. Fernández, C. A. Angelucci and J. Souza-Garcia, *J. Electroanal. Chem.*, 2021, **896**, 115198.
38 D. M. Morales, D. Jambrec, M. A. Kazakova, M. Braun, N. Sikdar, A. Koul, A. C. Brix, S. Seisel, C. Andronescu and W. Schuhmann, *ACS Catal.*, 2022, **12**, 982–992.
39 X. Yu, R. B. Araujo, Z. Qiu, E. Campos dos Santos, A. Anil, A. Cornell, L. G. M. Pettersson and M. Johnsson, *Adv. Energy Mater.*, 2022, **12**, 2103750.
40 J. Wu, J. Li, Y. Li, X. Y. Ma, W. Y. Zhang, Y. Hao, W. B. Cai, Z. P. Liu and M. Gong, *Angew. Chem., Int. Ed.*, 2021, **61**, 202113362.
41 L. Dong, G.-R. Chang, Y. Feng, X.-Z. Yao and X.-Y. Yu, *Rare Met.*, 2022, **41**, 1583–1594.

42 Z. He, J. Hwang, Z. Gong, M. Zhou, N. Zhang, X. Kang, J. W. Han and Y. Chen, *Nat. Commun.*, 2022, **13**, 3777.
43 N. Shilpa, A. Pandikassala, P. Krishnaraj, P. S. Walko, R. N. Devi and S. Kurungot, *ACS Appl. Mater. Interfaces*, 2022, **14**, 16222–16232.
44 Y. Pei, Z. Pi, H. Zhong, J. Cheng and F. Jin, *J. Mater. Chem. A*, 2022, **10**, 1309–1319.
45 Y. Xu, M. Liu, S. Wang, K. Ren, M. Wang, Z. Wang, X. Li, L. Wang and H. Wang, *Appl. Catal., B*, 2021, **298**, 120493.
46 X. Liu, Z. Fang, X. Teng, Y. Niu, S. Gong, W. Chen, T. J. Meyer and Z. Chen, *J. Energy Chem.*, 2022, **72**, 432–441.
47 X. Han, H. Sheng, C. Yu, T. W. Walker, G. W. Huber, J. Qiu and S. Jin, *ACS Catal.*, 2020, **10**, 6741–6752.
48 M. Braun, G. Behrendt, M. L. Krebs, P. Dimitri, P. Kumar, I. Sanjuán, S. Cychy, A. C. Brix, D. M. Morales, J. Hörlöck, B. Hartke, M. Muhler, W. Schuhmann, M. Behrens and C. Andronescu, *ChemElectroChem*, 2022, **9**, e202200267.
49 L. S. Oh, M. Park, Y. S. Park, Y. Kim, W. Yoon, J. Hwang, E. Lim, J. H. Park, S. M. Choi, M. H. Seo, W. B. Kim and H. J. Kim, *Adv. Mater.*, 2022, **34**, 2203285.
50 J. Chang, Y. Xiao, M. Xiao, J. Ge, C. Liu and W. Xing, *ACS Catal.*, 2015, **5**, 6874–6878.
51 Z. Li, H. Feng, M. Song, C. He, W. Zhuang and L. Tian, *Mater. Today Energy*, 2021, **20**, 100698.
52 X. Huang, Y. Zou and J. Jiang, *ACS Sustainable Chem. Eng.*, 2021, **9**, 14470–14479.
53 F. Yu, H. Zhou, Y. Huang, J. Sun, F. Qin, J. Bao, W. A. Goddard, 3rd, S. Chen and Z. Ren, *Nat. Commun.*, 2018, **9**, 2551.
54 Z. Zhao, D. E. Schipper, A. P. Leitner, H. Thirumalai, J.-H. Chen, L. Xie, F. Qin, M. K. Alam, L. C. Grabow, S. Chen, D. Wang, Z. Ren, Z. Wang, K. H. Whitmire and J. Bao, *Nano Energy*, 2017, **39**, 444–453.
55 J. F. Callejas, C. G. Read, E. J. Popczun, J. M. McEnaney and R. E. Schaak, *Chem. Mater.*, 2015, **27**, 3769–3774.
56 H. Yu, S. Qu, P.-R. Chen, K.-Q. Ou, J.-Y. Lin, Z.-H. Guo, L. Zheng, J.-K. Li, S. Huang, Y. Teng, L. Zou and J.-L. Song, *J. Hazard. Mater.*, 2022, **430**, 128351.
57 A. P. Grosvenor, S. D. Wik, R. G. Cavell and A. Mar, *Inorg. Chem.*, 2005, **44**, 8988–8998.
58 Z. Zheng, M. Retana, X. Hu, R. Luna, Y. H. Ikuhara and W. Zhou, *ACS Appl. Mater. Interfaces*, 2017, **9**, 16986–16994.
59 L. Ji, J. Wang, X. Teng, T. J. Meyer and Z. Chen, *ACS Catal.*, 2020, **10**, 412–419.
60 R. Shen, J. Xie, Y. Ding, S.-Y. Liu, A. Adamski, X. Chen and X. Li, *ACS Sustainable Chem. Eng.*, 2019, **7**, 3243–3250.
61 A. Saad, Z. Cheng, H. Shen, H. Guo, J. P. Attfield, T. Thomas and M. Yang, *Sustainable Energy Fuels*, 2021, **5**, 1366–1373.
62 S. Jin, *ACS Energy Lett.*, 2017, **2**, 1937–1938.
63 J. Hu, A. Al-Salihy, J. Wang, X. Li, Y. Fu, Z. Li, X. Han, B. Song and P. Xu, *Adv. Sci.*, 2021, **8**, 2103314.
64 H. Wang, Y. Zhou and S. Tao, *Appl. Catal., B*, 2022, **315**, 121588.
65 L. Yan, B. Zhang, J. Zhu, Y. Li, P. Tsiakaras and P. K. Shen, *Appl. Catal., B*, 2020, **265**, 118555.
66 B. Zhao, J. Liu, C. Xu, R. Feng, P. Sui, J.-X. Luo, L. Wang, J. Zhang, J.-L. Luo and X.-Z. Fu, *Appl. Catal., B*, 2021, **285**, 119800.
67 X. Xu, A. Cao, W. You, Z. Tao, L. Kang and J. Liu, *Small*, 2021, **17**, 2101725.
68 H. Y. Wang, S. F. Hung, H. Y. Chen, T. S. Chan, H. M. Chen and B. Liu, *J. Am. Chem. Soc.*, 2016, **138**, 36–39.
69 X. Deng, G. Y. Xu, Y. J. Zhang, L. Wang, J. Zhang, J. F. Li, X. Z. Fu and J. L. Luo, *Angew. Chem., Int. Ed.*, 2021, **60**, 20535–20542.
70 X. Huang, Y. Guo, Y. Zou and J. Jiang, *Appl. Catal., B*, 2022, **309**, 121247.
71 J. Yang, H. Liu, W. N. Martens and R. L. Frost, *J. Phys. Chem. C*, 2010, **114**, 111–119.
72 A. Moysiadou, S. Lee, C. S. Hsu, H. M. Chen and X. Hu, *J. Am. Chem. Soc.*, 2020, **142**, 11901–11914.
73 L. Reith, C. A. Triana, F. Pazoki, M. Amiri, M. Nyman and G. R. Patzke, *J. Am. Chem. Soc.*, 2021, **143**, 15022–15038.
74 M. Kong, H. Song and J. Zhou, *Adv. Energy Mater.*, 2018, **8**, 1801489.
75 M.-Q. Wang, C. Ye, H. Liu, M. Xu and S.-J. Bao, *Angew. Chem., Int. Ed.*, 2018, **57**, 1963–1967.
76 L. Yan, B. Zhang, J. Zhu, S. Zhao, Y. Li, B. Zhang, J. Jiang, X. Ji, H. Zhang and P. K. Shen, *J. Mater. Chem. A*, 2019, **7**, 14271–14279.
77 L. Zhang, G. Wang, X. Hao, Z. Jin and Y. Wang, *Chem. Eng. J.*, 2020, **395**, 125113.